

Cite this: *J. Mater. Chem. A*, 2015, 3, 12958

Oxygen storage capacity and thermal stability of the $\text{CuMnO}_2\text{--CeO}_2$ composite system†

Xiubing Huang, Chengsheng Ni, Guixia Zhao and John T. S. Irvine*

Fast and reversible oxygen diffusion in solid oxides depending on oxygen partial pressure at low temperatures is a promising strategy for improving the overall performance and service lifetime of many energy-related materials. However, the high energy required for the redox reaction of cations and their high thermodynamic barriers have impeded the realization of fast oxygen diffusion at low temperatures. Herein, we report enhanced oxygen diffusion and storage capacity of monoclinic crednerite CuMnO_2 at a lower temperature by surface modification with CeO_2 . The fast and reversible oxygen uptake/release can be attributed to CeO_2 that serves as a fast oxygen diffusion channel between bulk CuMnO_2 and the surrounding atmospheres. Importantly, the amount of CeO_2 in the $\text{CuMnO}_2\text{--CeO}_2$ composite system has a great effect on the total oxygen storage capacity and redox behaviour. Our findings could provide useful information for developing effective oxygen storage materials for wide energy-related applications.

Received 19th February 2015
Accepted 12th May 2015

DOI: 10.1039/c5ta01361e

www.rsc.org/MaterialsA

1. Introduction

Solid-state oxygen storage materials (OSMs) have attracted considerable attention due to their wide applications in numerous oxygen-related energy and environmental fields, such as three-way catalysts for the effective removal of automobile exhaust emissions (*e.g.*, NO_x , CO, and hydrocarbons).^{1,2} The development of OSMs is also crucial to the success of new energy technologies, such as oxygen enrichment to improve the efficiency of chemical looping combustion.³ Ideal OSMs for practical applications should satisfy certain requirements and possess some properties, including large oxygen storage capacity (OSC), quick absorption/desorption of oxygen and their dependence on temperature and/or oxygen partial pressure, and good reversibility.

The most widely investigated OSMs are based on ceria (*e.g.*, well-known $\text{Ce}_{1-x}\text{Zr}_x\text{O}_{2+\delta}$) due to the reversible redox reaction of $\text{Ce}^{3+}/\text{Ce}^{4+}$,^{2,4-8} however, their OSC is relatively small and usually achieved by the usage of reductive gas. Recently, oxides based on transition metals have attracted remarkable attention due to their excellent properties, such as their flexible oxidation states, various phase structures, possible substitutions, cationic and anionic non-stoichiometry, or lattice oxygen deficient in the framework.^{3,9-13} Their oxygen storage/release behaviour is generally based on the oxygen non-stoichiometry, which can be achieved by adjusting the surrounding oxygen partial pressure (*i.e.*, oxidative air, reductive H_2) or temperature.^{11,14} Among

OSMs based on transition-metals, extensive attention has been paid to delafossite-type oxides with the general formula CuMO_2 (M = trivalent cation) because of the low reductive/oxidative temperature of $\text{Cu}^{2+}/\text{Cu}^+$, remarkable oxygen uptake ability, wide potential applications, environmental-friendliness and abundance.¹⁵⁻¹⁷ However, only very limited work has been reported on the effect of trivalent cation species on the oxygen storage properties of the delafossite-type CuMO_2 oxides under oxidative/reductive atmospheres.¹⁵⁻¹⁷ For example, Sumio Kato, *et al.* reported that CuMnO_2 and CuFeO_2 exhibited larger OSC values at lower temperature than those of CuAlO_2 and CuGaO_2 ,¹⁵ and OSC values for $x = 0.1$ and 0.3 in $\text{CuFe}_{1-x}\text{Al}_x\text{O}_2$ were larger than that for $x = 0$ above 500°C .¹⁷ However, the full details of the phase-transformation process under oxidative/inert atmospheres and the effect of surface-modification by other metal oxides on the oxygen diffusion, oxygen storage capacity and thermal stability of CuMO_2 still remain not well-defined.

In the search for better OSMs, crednerite CuMnO_2 as an alternative phase to delafossite-type CuMO_2 seems to have great potential due to its changeable valence and low-temperature for oxygen uptake/release,^{15,18} and its wide applications, such as a hydrogen photo-evolution catalyst,¹⁹ a three-way catalyst for the removal of exhaust gases (*e.g.*, CO, NO_x),¹⁵ and hydrogen storage.²⁰ As reported by several research groups, crednerite CuMnO_2 exhibits a monoclinic structure at room temperature, which consists of edge-shared MnO_6 octahedra and two-coordinated Cu^+ cations at the interlayer sites, as represented in Fig. 1.^{15,19,21} This structure is closely related to the rhombohedral 3R delafossite structure of CuFeO_2 (*i.e.*, the Cu^+ cations linearly coordinating to two O ions, and the parallel O–Cu–O chains connecting Fe^{3+} cations to form two-dimensional sheets

School of Chemistry, University of St Andrews, St Andrews, Fife, UK. E-mail: jtsi@st-andrews.ac.uk; Fax: +44 (0)1334463808; Tel: +44 (0)133463680

† Electronic supplementary information (ESI) available: Additional XRD, TGA/DTA, HRTEM and FESEM images as well as TEM elemental mappings. See DOI: 10.1039/c5ta01361e



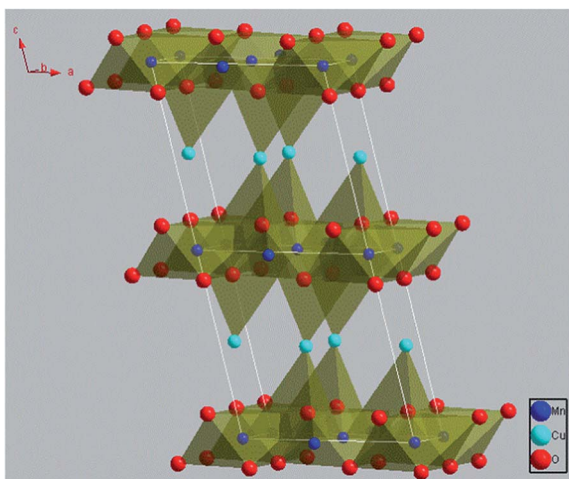


Fig. 1 Schematic illustration of the crystal structure of CuMnO_2 . The illustration was drawn with Diamond 3.1d software for crystal and molecular structure visualization.

of edge-shared FeO_6 octahedra), but with a distortion of the MnO_6 octahedron due to the Jahn–Teller effect of Mn^{3+} .²² However, it has been reported that $\text{Cu}_{1+x}\text{Mn}_{1-x}\text{O}_2$ ($0.08 < x < 0.12$) at high temperature can exhibit a delafossite-like phase with a hexagonal structure because the thermal expansion of the structure would result in a larger lattice distortion than that from the Jahn–Teller effect.^{23,24}

It is well known that multiple valences of Mn cations can co-exist in many Mn-containing compounds, which could be beneficial to the oxygen-storage properties.^{25–27} The valence of Mn in CuMnO_2 has been demonstrated to be +3, however the existence of Mn^{4+} in the nonstoichiometric $\text{Cu}_{1+x}\text{Mn}_{1-x}\text{O}_2$ oxides is also detected by XPS because the excess Cu atoms would occupy the octahedral site with Cu^{2+} while the electrical neutrality principle would result in the formation of mixed $\text{Mn}^{3+}/\text{Mn}^{4+}$.^{18,28} In addition, the $\text{Cu}_x\text{Mn}_{3-x}\text{O}_4$ spinel, one of the oxidation products of CuMnO_2 , has been reported to show the coexistence of $\text{Mn}^{3+}/\text{Mn}^{4+}$, implying a possible increase in the total oxygen uptake ability under an oxidative atmosphere.^{27,29,30} However, pure crednerite CuMnO_2 oxide is usually synthesized using the solid-state reaction at very high temperatures^{15,31,32} or the ion-exchange reaction with a long reaction time.³² Such a high reaction temperature or slow chemical conversion rate for reversible redox processes is impractical for many technological applications.¹⁸ Therefore, it is important to improve the oxygen diffusion ability and the overall oxygen storage capacity of crednerite CuMnO_2 at low temperatures.

CeO_2 has been widely investigated as a three-way catalyst or an oxygen promoter due to the fast oxygen ionic mobility between Ce^{4+} and Ce^{3+} in a reductive/oxidative atmosphere even though CeO_2 could retain its fluorite structure under oxidizing and mildly reducing atmospheres.^{33–37} CeO_2 has also been reported as an interlayer or electrolyte in the $\text{La}_{1-x}\text{Sr}_x\text{CoO}_{3-\delta}/\text{CeO}_2$ composite system to improve the oxygen ionic mobility, in which some chemical reactions can take place at the interfaces between perovskite and CeO_2 .^{38,39} Therefore, CeO_2 may function as an oxygen ionic mobility channel between oxides and their

surrounding atmosphere. Here, we investigated the $\text{CuMnO}_2\text{–CeO}_2$ composite system with the purpose of further optimizing the oxygen diffusion ability and overall oxygen storage capacity at low temperatures under alternating oxidative (*i.e.*, air or O_2) and inert (*i.e.*, Ar) atmospheres. Modifying the surfaces of CuMnO_2 with CeO_2 may bring in both benefits of CuMnO_2 and CeO_2 , thereafter adjusting their thermochemical properties (*e.g.*, redox properties, non-stoichiometry, oxygen exchange constant, and formation of oxygen vacancies), further enhancing their OSC and thermal stability. Our research results indicate that modifying CuMnO_2 with a small portion of CeO_2 (*e.g.*, the molar ratios of CeO_2 to CuMnO_2 smaller than 20%) can improve the oxygen storage capacity at low temperatures ($<600\text{ }^\circ\text{C}$) in a highly reversible manner.

2. Experimental section

2.1 Sample preparation

$\text{CuMnO}_2\text{–CeO}_2$ composites were prepared by a conventional Pechini method, followed by a solid state method. In a typical process, 10 mmol of $\text{Cu}(\text{NO}_3)_2 \cdot 2.5\text{H}_2\text{O}$ (98%) and 10 mmol of $\text{Mn}(\text{CH}_3\text{COO})_2 \cdot 4\text{H}_2\text{O}$ (98%) were dissolved in 100 mL of deionized H_2O under continuous stirring. A certain amount (0.5, 1.0, 2.0 or 4.0 mmol) of $\text{Ce}(\text{NO}_3)_3 \cdot 6\text{H}_2\text{O}$ (99.99%) was added into the above solution under stirring, followed by adding 20 mmol of citric acid monohydrate (99.95%) and 10 mL of ethylene glycol. After stirring for 4 h, the solvent was evaporated at $110\text{ }^\circ\text{C}$ to obtain a gel. After drying, the powder was ground and pre-fired at $500\text{ }^\circ\text{C}$ under static air for 1 h to obtain the precursor, then the precursor was pressed into pellets and fired at $960\text{ }^\circ\text{C}$ for 12 h under flowing argon. The obtained products were referred to as $\text{CuMnO}_2\text{–}x\text{CeO}_2$, in which x is the molar ratio percent of CeO_2 to CuMnO_2 (*i.e.*, $x = \text{mol of CeO}_2/\text{mol of CuMnO}_2 \times 100$).

2.2 Characterization

Structures of all samples were characterized by X-ray powder diffraction (XRD) on a PANalytical Empyrean Reflection Diffractometer with $\text{Cu K}\alpha$ irradiation ($\lambda = 0.15418\text{ nm}$). HRTEM images and TEM elemental mapping of samples were observed on a JEM-2011 Transmission Electron Microscope (TEM) with an acceleration voltage of 200 kV equipped with an X-ray Energy Dispersive spectrometer (EDS). The morphologies of all samples were observed on a JEOL JSM-6700 Field Scanning Electron Microscope (FESEM). The oxygen uptake behaviours of these samples were measured by thermogravimetric analysis (TGA) on a NETZSCH TG 209 instrument (NETZSCH-Geraetebau GmbH, Selb, Germany) with a TASC 414/3 controller. The measurements were carried out for 50 mg specimens up to $800\text{ }^\circ\text{C}$ with a heating rate of $10\text{ }^\circ\text{C min}^{-1}$ under air or O_2 with flowing rate 25 mL min^{-1} . In addition, the reversibility of the oxygen uptake/release was carried out in the following experiments: first increasing the temperature to $600\text{ }^\circ\text{C}$ under flowing O_2 gas, then switching the gas from O_2 to Ar with temperature from 600 to $900\text{ }^\circ\text{C}$; after cooling down to $300\text{ }^\circ\text{C}$ under flowing Ar, switching the gas from Ar to O_2 with temperature from 300



to 600 °C; this process was repeated between 300 and 900 °C 4 times. The thermal stability (weight and phase structural changes) of the as-prepared samples with temperature from room temperature to 1000 °C under flowing air was checked using a TGA/DTA technique carried out on a Stanton Redcroft STA-780 series thermal analyser.

3. Results and discussion

XRD patterns of these as-prepared $\text{CuMnO}_2-x\text{CeO}_2$ composites obtained by post-annealing at 960 °C for 12 h under flowing Ar are shown in Fig. 2. The XRD pattern for CuMnO_2 in Fig. 2a can be indexed to a pure monoclinic structure with a $C2/m$ space group. All the peaks are in good agreement with the JCPDS card no. 50-0860 for the crednerite phase. For the $\text{CuMnO}_2-x\text{CeO}_2$ composites, they are obviously composed of crednerite CuMnO_2 and fluorite CeO_2 , and no other impurity phases are observed. The XRD Rietveld refinements for CuMnO_2 and CeO_2 were carried out using GSAS software based on the monoclinic structure with the $C2/m$ space group and cubic structure with the $Fm\bar{3}m$ space group, respectively. The typical XRD patterns after final refinement for CuMnO_2 and $\text{CuMnO}_2-40\text{CeO}_2$ are shown in Fig. 3, further confirming the phase composition of CuMnO_2 and CeO_2 .²¹

Detailed lattice parameters for pure CuMnO_2 and $\text{CuMnO}_2-x\text{CeO}_2$ composites after Rietveld refinements are summarized in Table 1. There are no obvious changes in the lattice parameters a , b and c for CuMnO_2 and a for CeO_2 with the increasing CeO_2 amount up to $x = 40$ for the $\text{CuMnO}_2-x\text{CeO}_2$ composite, suggesting that CuMnO_2 and CeO_2 exist mainly as separate phases and there may be only a little contact between the surfaces. The HRTEM images of CuMnO_2 in $\text{CuMnO}_2-10\text{CeO}_2$ and $\text{CuMnO}_2-40\text{CeO}_2$ (Fig. S1†) show clear lattice fringes and these d spacings of 0.22 and 0.57 nm correspond to the (111) and (001) planes of CuMnO_2 , respectively.

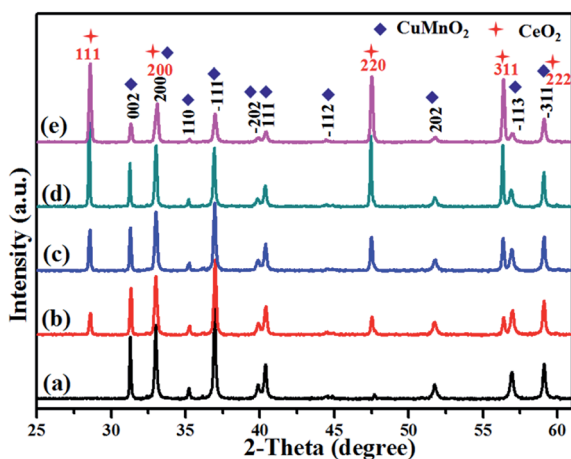


Fig. 2 XRD patterns of the as-prepared $\text{CuMnO}_2-x\text{CeO}_2$ (i.e., post-annealed at 960 °C under flowing Ar): (a) CuMnO_2 , (b) $\text{CuMnO}_2-5\text{CeO}_2$, (c) $\text{CuMnO}_2-10\text{CeO}_2$, (d) $\text{CuMnO}_2-20\text{CeO}_2$, and (e) $\text{CuMnO}_2-40\text{CeO}_2$.

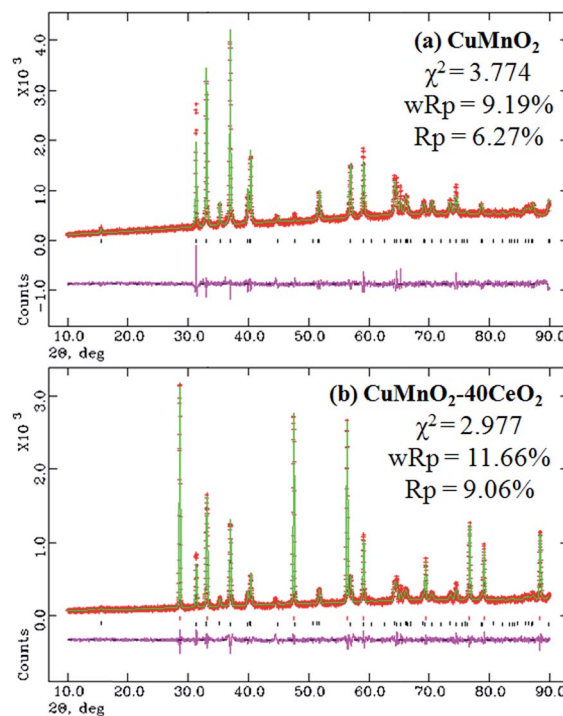
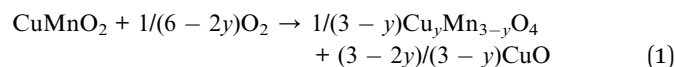


Fig. 3 XRD patterns after final Rietveld refinements for the as-prepared products: (a) CuMnO_2 and (b) $\text{CuMnO}_2-40\text{CeO}_2$.

The TEM elemental mappings of Cu, Mn, O and Ce for $\text{CuMnO}_2-10\text{CeO}_2$ (Fig. S2†) and $\text{CuMnO}_2-40\text{CeO}_2$ (Fig. S3†) also indicate the individual existence of CuMnO_2 and CeO_2 , as well as the inhomogeneous surface contact between CeO_2 and CuMnO_2 .

The oxygen uptake behaviours of the as-prepared $\text{CuMnO}_2-x\text{CeO}_2$ composites were investigated by TGA at temperature up to 800 °C under flowing air or O_2 . The results shown in Fig. 4 reveal a remarkable oxygen uptake capacity of this $\text{CuMnO}_2-x\text{CeO}_2$ composite system under an oxidative atmosphere, which corresponds to the following exothermic oxidation reaction:



The weight for all these samples starts to increase at about 300 °C, due to the increase in the oxygen content, accompanied by the oxidation of Cu^+ and/or Mn^{3+} . Pure CuMnO_2 had a continuous and smooth weight increase with increasing temperature from 300 to 800 °C, reaching the maximum value of 5.475 wt% at 800 °C under both flowing air and O_2 , corresponding to the formation of spinel $\text{Cu}_{1.058}\text{Mn}_{1.942}\text{O}_4$. For pure CuMnO_2 and $\text{CuMnO}_2-x\text{CeO}_2$ composites, the oxygen uptake rate in air is a bit slower than that in O_2 and the maximum oxygen uptake amount in air is also a bit smaller than that in O_2 , in which $\text{CuMnO}_2-5\text{CeO}_2$ exhibits the most weight increase, reaching 6.169 wt% at 591 °C under flowing O_2 and 6.031 wt% at 620 °C under flowing air, respectively, suggesting that higher oxygen partial pressure would enhance the oxygen uptake



Table 1 Lattice parameters of the as-prepared $\text{CuMnO}_2-x\text{CeO}_2$ obtained from Rietveld refinements using GSAS software

As-prepared sample	Composition	a (Å)	b (Å)	c (Å)	Cell volume (Å ³)	β
CuMnO_2	CuMnO_2	5.592(3)	2.883(1)	5.892(3)	92.1(1)	104.03(3)
$\text{CuMnO}_2-5\text{CeO}_2$	CuMnO_2	5.597(3)	2.883(1)	5.892(3)	92.2(1)	104.00(4)
	CeO_2		5.412(2)		158.5(2)	
$\text{CuMnO}_2-10\text{CeO}_2$	CuMnO_2	5.593(1)	2.883(6)	5.892(1)	92.19(3)	104.06(3)
	CeO_2		5.412(1)		158.5(2)	
$\text{CuMnO}_2-20\text{CeO}_2$	CuMnO_2	5.589(2)	2.882(1)	5.891(2)	92.08(8)	104.08(4)
	CeO_2		5.411(1)		158.4(1)	
$\text{CuMnO}_2-40\text{CeO}_2$	CuMnO_2	5.597(3)	2.883(1)	5.891(3)	92.24(9)	104.06(7)
	CeO_2		5.412(2)		158.5(3)	

ability at lower temperatures. With the further increase of CeO_2 amount in the composite, the maximum OSC decreased, which can be attributed to the offset effect of CeO_2 since the weight increase is mainly caused by the oxidation of Cu^+ and/or Mn^{3+} in CuMnO_2 while CeO_2 could maintain its fluorite-type structure under an inert atmosphere,^{40,41} as determined by the XRD results in Fig. 2. After reaching the maximum weight at around 600 °C, further increasing the temperature to 800 °C results in a slight and smooth weight decrease (<0.14 wt%) for all these CeO_2 -modified CuMnO_2 samples, which can be attributed to the composition adjustment of spinel $\text{Cu}_y\text{Mn}_{3-y}\text{O}_4$ with temperature.¹⁸ These results also indicate that CeO_2 -modification would favour the oxygen mobility in CuMnO_2 and the formation of spinel $\text{Cu}_y\text{Mn}_{3-y}\text{O}_4$ with more Mn^{4+} at lower temperatures. It should be noted that the oxygen uptake in CuMnO_2 and $\text{CuMnO}_2-x\text{CeO}_2$ composites mainly comes from the oxidation of CuMnO_2 to CuO and spinel $\text{Cu}_y\text{Mn}_{3-y}\text{O}_4$. Assuming that the total weight increase only comes from the oxidation of CuMnO_2 , the composition of spinel $\text{Cu}_y\text{Mn}_{3-y}\text{O}_4$ at the maximum weight under flowing O_2 can be calculated based on eqn (1) to be $\text{Cu}_{1.370}\text{Mn}_{1.630}\text{O}_4$ for the $\text{CuMnO}_2-5\text{CeO}_2$ starting mix, $\text{Cu}_{1.317}\text{Mn}_{1.683}\text{O}_4$ for $\text{CuMnO}_2-10\text{CeO}_2$, $\text{Cu}_{1.356}\text{Mn}_{1.644}\text{O}_4$ for $\text{CuMnO}_2-20\text{CeO}_2$ and $\text{Cu}_{1.316}\text{Mn}_{1.684}\text{O}_4$ for $\text{CuMnO}_2-40\text{CeO}_2$, while the composition of spinels at the

maximum weight under flowing air can be calculated to be $\text{Cu}_{1.332}\text{Mn}_{1.668}\text{O}_4$ for $\text{CuMnO}_2-5\text{CeO}_2$, $\text{Cu}_{1.296}\text{Mn}_{1.704}\text{O}_4$ for $\text{CuMnO}_2-10\text{CeO}_2$, $\text{Cu}_{1.310}\text{Mn}_{1.690}\text{O}_4$ for $\text{CuMnO}_2-20\text{CeO}_2$ and $\text{Cu}_{1.268}\text{Mn}_{1.732}\text{O}_4$ for $\text{CuMnO}_2-40\text{CeO}_2$, respectively. These calculation results suggest that higher oxygen partial pressure favours the formation of spinels with more Mn^{4+} from the oxidation of $\text{CuMnO}_2-x\text{CeO}_2$ composites.

XRD patterns of the oxygenated CuMnO_2 and $\text{CuMnO}_2-x\text{CeO}_2$ composites after the TGA test up to 800 °C under flowing air are shown in Fig. 5. While CeO_2 in these oxygenated $\text{CuMnO}_2-x\text{CeO}_2$ composites still maintained its fluorite-type cubic structure, CuMnO_2 was oxidized to CuO and spinel $\text{Cu}_y\text{Mn}_{3-y}\text{O}_4$ oxides, in good agreement with the TGA analysis in Fig. 4 and previous reported results.¹⁸ The lattice parameters of CeO_2 and spinel $\text{Cu}_y\text{Mn}_{3-y}\text{O}_4$ in the oxygenated CuMnO_2 and $\text{CuMnO}_2-x\text{CeO}_2$ composites after the TGA test up to 800 °C in flowing air were refined from the XRD results in Fig. 5 using GSAS software and are summarized in Table 2. The lattice parameters of CeO_2 in the oxygenated $\text{CuMnO}_2-x\text{CeO}_2$ composites are a bit smaller than those of the as-prepared $\text{CuMnO}_2-x\text{CeO}_2$ composites (as shown in Table 1), indicating the possible doping of Mn and/or Cu in the lattice of CeO_2 after oxidation. In addition, the lattice parameters of spinel $\text{Cu}_y\text{Mn}_{3-y}\text{O}_4$ in the oxygenated $\text{CuMnO}_2-x\text{CeO}_2$ composites are also slightly smaller than those of oxygenated pure CuMnO_2 ,

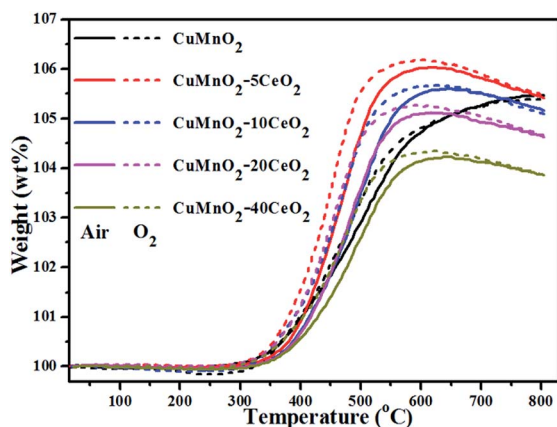


Fig. 4 TGA curves of the as-prepared $\text{CuMnO}_2-x\text{CeO}_2$ samples (*i.e.*, post-annealed at 960 °C under flowing Ar for 12 h) under flowing air or pure O_2 with 25 mL min^{-1} from room temperature to 800 °C. The solid lines are the TGA curves under air and the short dashed lines are the TGA curves under pure O_2 .

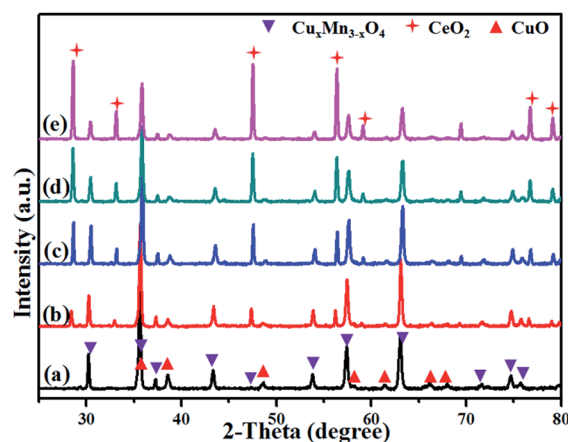


Fig. 5 XRD patterns after the TGA test from room temperature to 800 °C under flowing air: (a) CuMnO_2 , (b) $\text{CuMnO}_2-5\text{CeO}_2$, (c) $\text{CuMnO}_2-10\text{CeO}_2$, (d) $\text{CuMnO}_2-20\text{CeO}_2$, and (e) $\text{CuMnO}_2-40\text{CeO}_2$.



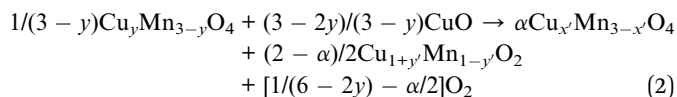
Table 2 Lattice parameters of oxygenated $\text{CuMnO}_2-x\text{CeO}_2$ in Fig. 5 from Rietveld refinements using GSAS software

Oxygenated $\text{CuMnO}_2-x\text{CeO}_2$	Composition	a (Å)	Cell volume (Å ³)
CuMnO_2	$\text{Cu}_y\text{Mn}_{3-y}\text{O}_4$	8.317(2)	575.30(7)
$\text{CuMnO}_2-5\text{CeO}_2$	$\text{Cu}_y\text{Mn}_{3-y}\text{O}_4$ CeO_2	8.307(2) 5.407(8)	573.23(4) 158.14(7)
$\text{CuMnO}_2-10\text{CeO}_2$	$\text{Cu}_y\text{Mn}_{3-y}\text{O}_4$ CeO_2	8.311(5) 5.409(1)	574.06(3) 158.26(1)
$\text{CuMnO}_2-20\text{CeO}_2$	$\text{Cu}_y\text{Mn}_{3-y}\text{O}_4$ CeO_2	8.309(4) 5.410(6)	573.64(9) 158.39(3)
$\text{CuMnO}_2-40\text{CeO}_2$	$\text{Cu}_y\text{Mn}_{3-y}\text{O}_4$ CeO_2	8.312(2) 5.410(2)	574.27(1) 158.35(8)

indicating the higher Cu/Mn ratios in the spinel $\text{Cu}_y\text{Mn}_{3-y}\text{O}_4$ in the oxygenated $\text{CuMnO}_2-x\text{CeO}_2$ composites as the smaller ionic radii of Cu^{2+} than that of Mn^{2+} would result in a decrease of lattice parameters when copper ions replace manganese ions on tetrahedral sites.

To further check their thermal stability with temperature under flowing air, we treated the as-prepared samples (*i.e.*, post-annealed at 960 °C for 12 h under flowing Ar) from room temperature up to 1000 °C with heating and cooling rates of ± 10 °C min^{-1} under flowing air, as shown in Fig. 6. As discussed in aforementioned paragraphs, the as-prepared samples can start to take up oxygen near 300 °C and reach the maximum values at near 600 °C for $\text{CuMnO}_2-x\text{CeO}_2$ composites and 800 °C for pure CuMnO_2 , respectively. On further heating, these samples exhibit a steep weight loss from 960 °C accompanied by an endothermic peak in the DTA curves, as shown in Fig. S4.† Such behaviour can be attributed to the transformation of spinels and CuO back into a crednerite $\text{Cu}_{1+y'}\text{Mn}_{1-y'}\text{O}_2$ phase, accompanied by the release of O_2 .^{18,32} During the cooling process under flowing air from 1000 °C, there is a sharp continuous weight increase up to around 880 °C, which can be attributed to the re-oxidation of the crednerite phase to CuO and spinel oxides. The slight weight increase from 880 to 600 °C

can be attributed to the composition adjustment of spinels with the cooling temperature, as determined by XRD shown in Fig. S5.† Notably, their weights at 1000 °C are higher than their pristine counterparts, suggesting that CuO and spinel $\text{Cu}_y\text{Mn}_{3-y}\text{O}_4$ at high temperature under air can be converted to $\text{Cu}_{1+y'}\text{Mn}_{1-y'}\text{O}_2$ rather than CuMnO_2 according to eqn (2).



where $\alpha = 2y'/(3+3y'-2x')$.

The TGA behaviours of the oxygenated $\text{CuMnO}_2-x\text{CeO}_2$ composites (*i.e.*, after the TGA test up to 800 °C under flowing O_2) with temperature up to 900 °C under flowing argon are displayed in Fig. 7. The results show that all these samples are stable up to around 600 °C under flowing argon. Further increasing temperature would lead to a continuous weight loss (<1.2 wt%) up to about 790 °C, in which the oxygenated $\text{CuMnO}_2-5\text{CeO}_2$ exhibited the most weight loss and the total weight loss decreased with the increase of CeO_2 . The small weight loss can be attributed to the removal of oxygen in spinels. At temperatures higher than 790 °C, these sharp weight losses are attributed to the further removal of oxygen to form crednerite $\text{Cu}_{1+y'}\text{Mn}_{1-y'}\text{O}_2$.³¹ To further support this conclusion, we treated the oxygenated CuMnO_2 , $\text{CuMnO}_2-5\text{CeO}_2$ and $\text{CuMnO}_2-20\text{CeO}_2$ under flowing argon at 900 °C for 2 h and their XRD patterns shown in Fig. S6† indicate the reformation of the crednerite CuMnO_2 structure. The total weight losses for the oxygenated $\text{CuMnO}_2-5\text{CeO}_2$, $\text{CuMnO}_2-10\text{CeO}_2$ and $\text{CuMnO}_2-20\text{CeO}_2$ are higher than that for oxygenated CuMnO_2 . The enhanced oxygen mobility and storage capacity of the $\text{CuMnO}_2-x\text{CeO}_2$ composite system can be attributed to the synergistic effect between CuMnO_2 and CeO_2 , in which CeO_2 can act as an oxygen transfer channel or oxygen promoter dependent on temperature and/or oxygen partial pressures. The possible doping or exsolution of Cu/Mn into or from the lattice of CeO_2 on the surface depending on the temperature and oxygen partial pressure may also contribute to the enhanced

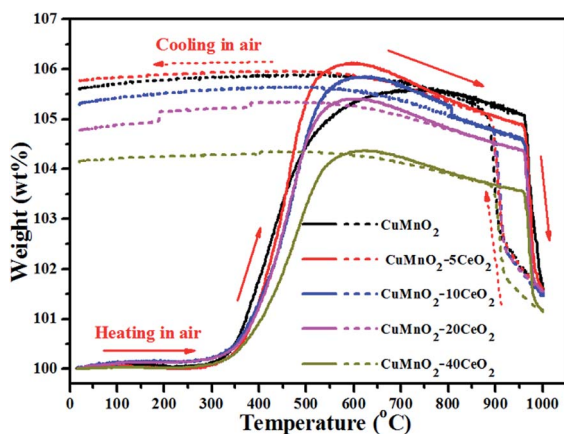


Fig. 6 TGA curves of the as-prepared $\text{CuMnO}_2-x\text{CeO}_2$ samples (*i.e.*, post-annealed at 960 °C for 12 h under flowing Ar) from room temperature up to 1000 °C with heating and cooling rates of 10 °C min^{-1} under flowing air.

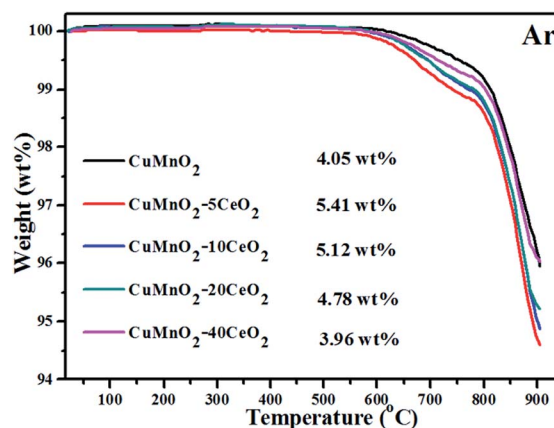


Fig. 7 TGA curves of oxidized $\text{CuMnO}_2-x\text{CeO}_2$ samples (*i.e.*, after the TGA test up to 800 °C under flowing O_2) from room temperature to 900 °C under flowing argon with 25 mL min^{-1} .



performance. Therefore, with the surface modification of CeO_2 , CuMnO_2 can take up oxygen from CeO_2 rather than directly from the surrounding O_2 atmosphere and *vice versa*, under an inert Ar atmosphere, CuO and spinel $\text{Cu}_y\text{Mn}_{3-y}\text{O}_4$ can release oxygen to the CeO_2 lattice and then to the surroundings, rather than directly to the surroundings.

From the TGA data in Fig. 4, it appears that these CeO_2 -modified CuMnO_2 oxides can be oxidized from 300 °C and reach the maximum weight at around 600 °C under flowing O_2 , while the oxygenated samples can start to release oxygen from 600 °C under flowing argon based on the TGA results in Fig. 7. These results indicate that CeO_2 -modified CuMnO_2 oxides can cause either oxygen uptake or release depending on the temperature and/or oxygen partial pressure. Thus, remarkable oxygen uptake/release behaviours are expected *via* adjusting the temperature and oxygen partial pressure. As demonstrated in Fig. 8, CuMnO_2 and CeO_2 -modified CuMnO_2 oxides can take up/release a large amount of oxygen in which CuMnO_2 -5 CeO_2 exhibits the highest OSC (*ca.* 6.0 wt%) and CuMnO_2 -20 CeO_2 shows the best reversibility under the alternating O_2 and argon between 300 and 900 °C for four cycles, indicating that CeO_2 modification would improve the oxygen storage capacity as well as the reversibility of CuMnO_2 . The OSC and reversibility would become worse with the increasing cycle times, as shown in Fig. S7,[†] but the final weight after each treatment under flowing argon during the cycles almost remains the same, indicating that the gradual weight loss may be due to the formation of spinels with less Mn^{4+} during the oxidation process with the increasing cycling times. As shown in Fig. S8,[†] after a nine cycle test under alternating O_2 and argon, CuMnO_2 -5 CeO_2 still contains crednerite CuMnO_2 and fluorite CeO_2 phases; however, there are obvious CeO_2 nanoparticles on the CuMnO_2 surface, in comparison to the FESEM images in Fig. S9.[†] The TEM results for CuMnO_2 -10 CeO_2 after the TGA test, as shown in Fig. S10,[†] also indicate the appearance of CeO_2 nanoparticles on the surface of CuMnO_2 , which resulted in a worse performance for the oxidation of CuMnO_2 . The TEM elemental

mapping results for CuMnO_2 -10 CeO_2 in Fig. S10[†] suggest that some Cu is doped into the lattice of CeO_2 while Mn is still in CuMnO_2 , which can be explained by the bigger ionic radius of Cu^{2+} (0.73 Å) and Cu^+ (0.77 Å) than that of Mn^{3+} (0.58 Å) and Mn^{4+} (0.53 Å).

4. Conclusions

In conclusion, we found that fast and reversible oxygen mobility, and increased oxygen storage capacity of crednerite CuMnO_2 could be achieved at reduced temperatures (*ca.* 600 °C) by surface modification with CeO_2 at an amount less than 20 mol% in the CuMnO_2 - CeO_2 composite system. The fast and reversible oxygen uptake/release and increased oxygen storage capacity at lower temperatures can be attributed to the synergistic effect of CeO_2 as an oxygen diffusion channel between bulk CuMnO_2 and the surrounding atmospheres, favouring the reversible formation of spinels at lower temperatures. Our findings reported here could provide a pathway for the design and development of effective oxygen storage materials for a range of energy-synergetic related applications at low temperatures.

Acknowledgements

The authors gratefully thank the Engineering and Physical Sciences Research Council (EPSRC) platform grant EP/I022570/1 and EP/I022570/2 for financial support.

Notes and references

- 1 H. C. Yao and Y. F. Y. Yao, *J. Catal.*, 1984, **86**, 254–265.
- 2 C. E. Hori, H. Permana, K. Y. S. Ng, A. Brenner, K. More, K. M. Rahmoeller and D. Belton, *Appl. Catal., B*, 1998, **16**, 105–117.
- 3 T. Motohashi, Y. Hirano, Y. Masubuchi, K. Oshima, T. Setoyama and S. Kikkawa, *Chem. Mater.*, 2013, **25**, 372–377.
- 4 M. Ozawa, M. Kimura and A. Isogai, *J. Alloys Compd.*, 1993, **193**, 73–75.
- 5 A. Gupta, U. V. Waghmare and M. S. Hegde, *Chem. Mater.*, 2010, **22**, 5184–5198.
- 6 M. P. Yeste, J. C. Hernandez-Garrido, D. C. Arias, G. Blanco, J. M. Rodriguez-Izquierdo, J. M. Pintado, S. Bernal, J. A. Perez-Omil and J. J. Calvino, *J. Mater. Chem. A*, 2013, **1**, 4836–4844.
- 7 X. Wang, G. Lu, Y. Guo, L. Jiang, Y. Guo and C. Li, *J. Mater. Sci.*, 2009, **44**, 1294–1301.
- 8 Q. Dong, S. Yin, C. Guo, T. Kimura and T. Sato, *RSC Adv.*, 2012, **2**, 12770–12774.
- 9 S. Remsen and B. Dabrowski, *Chem. Mater.*, 2011, **23**, 3818–3827.
- 10 O. Parkkima, H. Yamauchi and M. Karppinen, *Chem. Mater.*, 2013, **25**, 599–604.
- 11 S. Carter, A. Selcuk, R. J. Chater, J. Kajda, J. A. Kilner and B. C. H. Steele, *Solid State Ionics*, 1992, **53–56**, 597–605.

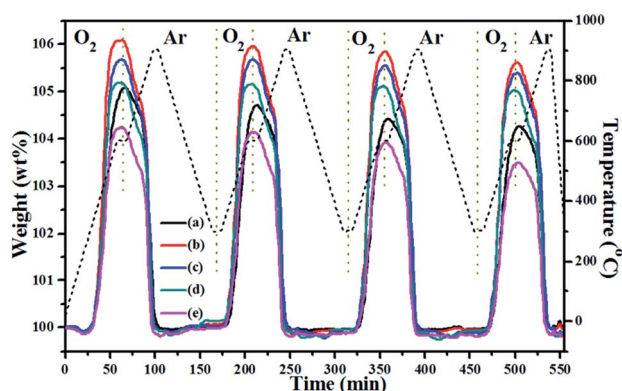


Fig. 8 TGA curves of the as-prepared CuMnO_2 - $x\text{CeO}_2$ samples (*i.e.*, post-annealed at 960 °C for 12 h under flowing Ar) under alternating O_2 and argon. The samples were first oxidized under O_2 to 600 °C, then the gas was switched to argon and the temperature was increased to 900 °C. After being cooled down to 300 °C under argon, the gas was then switched back to O_2 and oxidized to 600 °C.



- 12 M. Cherry, M. S. Islam and C. R. A. Catlow, *J. Solid State Chem.*, 1995, **118**, 125–132.
- 13 J. W. Lekse, S. Natesakhawat, D. Alfonso and C. Matranga, *J. Mater. Chem. A*, 2014, **2**, 2397–2404.
- 14 H. Jeon, W. S. Choi, M. D. Biegalski, C. M. Folkman, I. C. Tung, D. D. Fong, J. W. Freeland, D. Shin, H. Ohta, M. F. Chisholm and H. N. Lee, *Nat. Mater.*, 2013, **12**, 1057–1063.
- 15 S. Kato, R. Fujimaki, M. Ogasawara, T. Wakabayashi, Y. Nakahara and S. Nakata, *Appl. Catal., B*, 2009, **89**, 183–188.
- 16 S. Kato, H. Sato, M. Ogasawara, T. Wakabayashi, Y. Nakahara and S. Nakata, *Solid State Sci.*, 2012, **14**, 177–181.
- 17 S. Kato, S. Suzuki, R. Kawashima, M. Ogasawara, T. Wakabayashi, Y. Nakahara and S. Nakata, *J. Mater. Sci.*, 2013, **48**, 8077–8083.
- 18 M. Trari, J. Töpfer, P. Dordor, J. C. Grenier, M. Pouchard and J. P. Doumerc, *J. Solid State Chem.*, 2005, **178**, 2751–2758.
- 19 Y. Bessekhoud, M. Trari and J. P. Doumerc, *Int. J. Hydrogen Energy*, 2003, **28**, 43–48.
- 20 S. A. M. Abdel-Hameed, F. H. Margha and A. A. El-Meligi, *Int. J. Energy Res.*, 2014, **38**, 459–465.
- 21 Y. Bessekhoud, Y. Gabes, A. Bouguelia and M. Trari, *J. Mater. Sci.*, 2007, **42**, 6469–6476.
- 22 J. Topfer, M. Trari, P. Gravereau, J. P. Chaminade and J. P. Doumerc, *Z. Kristallogr.*, 1995, **210**, 184–187.
- 23 F. C. M. Driessens and G. D. Rieck, *Z. Anorg. Allg. Chem.*, 1967, **351**, 48–62.
- 24 P. Wei, M. Bieringer, L. D. Cranswick and A. Petric, *J. Mater. Sci.*, 2010, **45**, 1056–1064.
- 25 J. Li, S. Xiong, X. Li and Y. Qian, *Nanoscale*, 2013, **5**, 2045–2054.
- 26 N. K. Radhakrishnan and A. B. Biswas, *Phys. Status Solidi A*, 1977, **44**, 45–49.
- 27 D. P. Shoemaker, J. Li and R. Seshadri, *J. Am. Chem. Soc.*, 2009, **131**, 11450–11457.
- 28 H. Y. Chen and D. J. Hsu, *J. Alloys Compd.*, 2014, **598**, 23–26.
- 29 I. N. Dubrovina, V. F. Balakirev and A. V. Antonov, *Inorg. Mater.*, 2001, **37**, 76–81.
- 30 E. Ríos, S. Abarca, P. Daccarett, H. Nguyen Cong, D. Martel, J. F. Marco, J. R. Gancedo and J. L. Gautier, *Int. J. Hydrogen Energy*, 2008, **33**, 4945–4954.
- 31 A. P. Amrute, Z. Łodziana, C. Mondelli, F. Krumeich and J. Pérez-Ramírez, *Chem. Mater.*, 2013, **25**, 4423–4435.
- 32 B. Bellal, B. Hadjarab, N. Benreguia, Y. Bessekhoud and M. Trari, *J. Appl. Electrochem.*, 2011, **41**, 867–872.
- 33 Z. Liu, Z. Wu, X. Peng, A. Binder, S. Chai and S. Dai, *J. Phys. Chem. C*, 2014, **118**, 27870–27877.
- 34 L. Shi, W. Chu, F. Qu and S. Luo, *Catal. Lett.*, 2007, **113**, 59–64.
- 35 A. Hornés, A. B. Hungria, P. Bera, A. L. Cámara, M. Fernández-García, A. Martínez-Arias, L. Barrio, M. Estrella, G. Zhou, J. J. Fonseca, J. C. Hanson and J. A. Rodriguez, *J. Am. Chem. Soc.*, 2009, **132**, 34–35.
- 36 S. D. Senanayake, D. Stacchiola and J. A. Rodriguez, *Acc. Chem. Res.*, 2013, **46**, 1702–1711.
- 37 I. Moog, C. Feral-Martin, M. Duttine, A. Wattiaux, C. Prestipino, S. Figueroa, J. Majimel and A. Demourgues, *J. Mater. Chem. A*, 2014, **2**, 20402–20414.
- 38 E. Y. Konyshcheva, S. M. Francis, J. T. S. Irvine, A. Rolle and R.-N. Vannier, *J. Mater. Chem.*, 2011, **21**, 15511–15520.
- 39 E. Konyshcheva, R. Blackley and J. T. S. Irvine, *Chem. Mater.*, 2010, **22**, 4700–4711.
- 40 A. S. Ivanova, *Kinet. Catal.*, 2009, **50**, 797–815.
- 41 Y. Zhou and M. N. Rahaman, *Acta Mater.*, 1997, **45**, 3635–3639.

